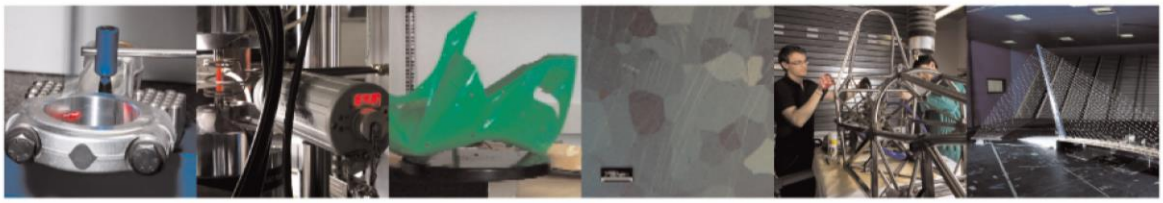

Characterization of in-situ measurements based on layerwise imaging in laser powder bed fusion

Caltanissetta, F.; Grasso, M.; Petrò, S.; Colosimo, B. M.

DIPARTIMENTO DI MECCANICA ■ POLITECNICO DI MILANO
via G. La Masa, 1 ■ 20156 Milano ■ EMAIL (PEC): pecmecc@cert.polimi.it
http://www.mecc.polimi.it
Rev. 0

Characterization of In-Situ Measurements based on Layerwise Imaging in Laser Powder Bed Fusion

Fabio Caltanissetta, Marco Grasso*, Stefano Petrò, Bianca Maria Colosimo

Dipartimento di Meccanica, Politecnico di Milano, Via La Masa 1, 20156

**corresponding author, marcoluigi.grasso@polimi.it*

Abstract – The layerwise production paradigm entailed in laser powder bed fusion (LPBF) offers the opportunity to acquire a wide range of information about the process stability and the part quality while the part is being manufactured. Different authors pointed out that high-resolution imaging of each printed layer combined with image segmentation methods can be used to detect powder recoating errors together with surface and geometrical defects. The paper presents the first study aimed at characterizing the accuracy of in-situ contour identification in LPBF layerwise images by means of a measurement system performance characterization. Different active contours segmentation methods are compared, and the sources of variability of the resulting measurements are investigated in terms of repeatability, part-to-part and build-to-build variability. The study also analyses and compares the sensitivity of in-situ measurements to different lighting conditions and laser scan directions. The results show that, by combining appropriate image pre-processing and segmentation algorithms with suitable lighting configurations, a high measurement repeatability can be achieved, i.e., a pure error that is up to one order of magnitude lower than the total measurement variability. This performance enables the detection of major geometric deviations and it paves the way to the design of statistical in-situ quality monitoring tools that rely on layerwise image segmentation.

Keywords: Additive Manufacturing; Laser Powder Bed Fusion; image segmentation; active contours; measurement accuracy.

1. INTRODUCTION

The laser powder bed fusion (LPBF) technology has attracted an increasing interest in different industrial sectors for the production of innovative structures, complex shapes and customized parts [1 – 3]. Compared to other metal additive manufacturing processes, it provides high accuracy and resolution combined with good mechanical and microstructural properties, which make it suitable for applications characterized by stringent

quality requirements. At the same time, those requirements impose the need for reliable and robust in-situ monitoring tools able to quickly detect process defects and to reduce the time and costs associated to post-process quality inspections. To this aim, the layerwise production paradigm offers the opportunity to gather a large amount of data while the part is being produced. An increasing number of studies have been devoted to the development of in-situ sensing and monitoring methodologies in LPBF in the recent years [4 – 6]. The different methods proposed in the literature differ in terms of measured quantities, also known as process signatures, and in terms of sensing setup. In particular, the LPBF technology enables two major sensing configurations, namely co-axial sensors, which exploit the optical path of the laser to monitor the melt pool properties, and off-axial sensors, which allow measuring additional quantities by means of a much larger field of view and on different spatial/temporal scales. This study focuses on the off-axial sensing approach, using high-resolution cameras to acquire layerwise images of the powder bed, possibly before and after the laser scanning of the slice. As pointed out by various authors (Abdelraham *et al*. [7]; Li *et al*. [8]; Aminzadeh and Kurfess [9]; Foster *et al*. [10]; Kleszczynski *et al*. [11]; zur Jacobsmühlen *et al*. [12 – 13]), layerwise imaging in LPBF could be used to detect in-plane and out-of-plane defects, reconstruct the 3D geometry of the part on a layer-by-layer basis, detect powder contamination flaws and other powder recoating errors. The specific focus of our study regards the possibility of quickly detecting major deviations between the in-situ detected contours of foreground regions and the nominal geometry of the slice. A motivating example is shown in Fig. 1, which refers to the LPBF of a complex AISI 316L shape [14-15]. A local recoating error occurred in one layer and repeated for few following layers. Because of the lack of powder over a portion of the scanned region, a discontinuity in the material was produced, leading to the major delamination shown in Fig. 1 (bottom-right panel), which was further inflated by thermal stresses in the part. Fig. 1 shows that by combining pre-scan and post-scan images during the LPBF process and comparing the in-situ detected region with the nominal shape of the slice it could be possible to anticipate the detection of such a severe defect (the mismatch between the two regions is highlighted in blue in Fig. 1). This capability is particularly appealing from an industrial implementation viewpoint, as almost all LBPF systems are already equipped with off-axial cameras that capture pictures of each layer during the process [4].

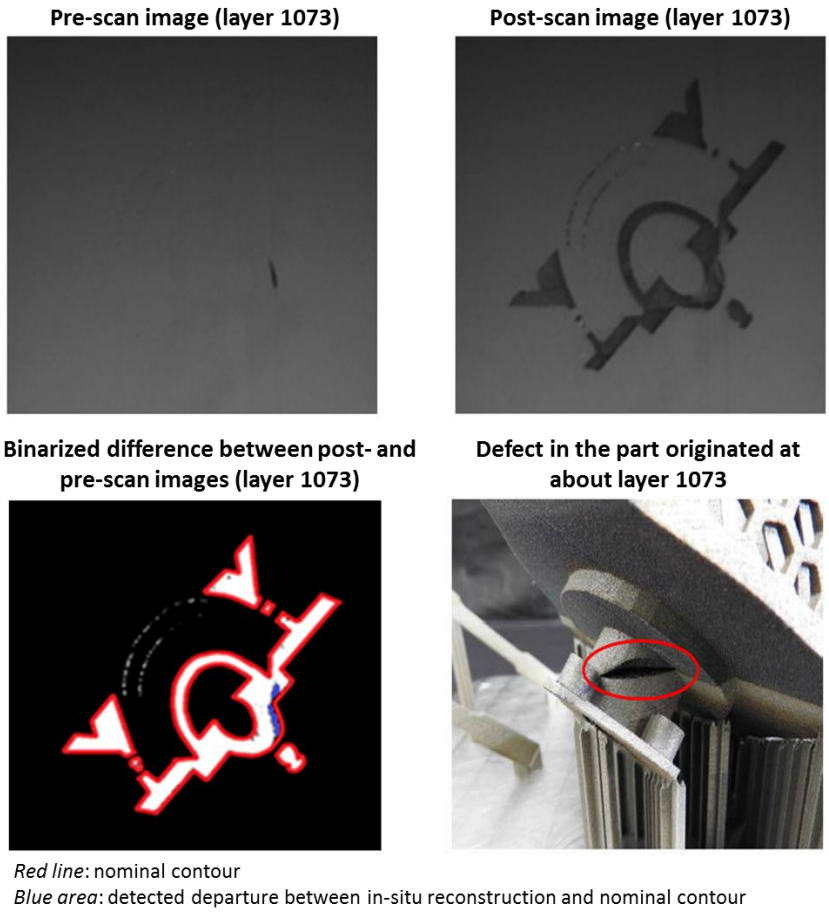

Fig. 1 – Example of macroscopic defect in an AISI 316L part produced by using a Renishaw AM250 LPBF system, and the possibility of in-situ defect detection based on a combination of pre-scan and post-scan images for contour reconstruction and comparison against the nominal geometry [14-15]

It is worth noting that part dimensions and geometries measured in-situ are not representative of the final dimensions and geometry of the as-built part, because of shrinkage and thermal stress-induced distortions that cannot be captured on a layer-by-layer basis. However, if a major departure from the expected shape is observed in one layer, it is worth signalling it as soon as possible, since it may be representative of a defect that cannot be recovered as the process goes on. Fig. 1 highlights that an accurate image segmentation enables such defect detection ability. In this framework, understanding the accuracy of in-situ contour identification based on layerwise image segmentation represents a key issue to characterize the performance of the measurement system to identify defects and departures from a known reference. This motivated the present paper, which represents the first measurement system performance characterization applied to layerwise imaging in LPBF. To this aim, we propose an experimental procedure that relies on the dimensional

measurement of simple geometrical features. The in-situ optical measurement in one layer was compared with a reference defined by means of ex-situ optical measurements of the same layer (both the in-situ and ex-situ images were acquired at room temperature to avoid mismatches caused by shrinkage effects). The sources of variability that affected the measurement accuracy were investigated by means of a random effect model to decompose the total variability of the measurement into part-to-part variability, build-to-build variability and pure error (measurement repeatability). The study also analyses and compares the sensitivity of the image segmentation and the resulting measurement with respect to different illumination conditions and laser scan directions.

Among the wide number of image segmentation techniques available in the literature [16], the present study focuses on a specific category of methods known as *active contours* [17 – 19]. They iteratively modify an initial boundary defined by a closed curve until a so-called segmentation-dependent energy functional is minimized. Active contours methods were demonstrated to be quite effective in segmenting images similar to LPBF layer images, including noisy patterns, non-homogeneous pixel intensity patterns and not well-defined edges [17 – 18]. Moreover, they yield connected contours, whereas edge detection methods often produce discontinuous boundaries. One major drawback of active contours consists of the need to set a contour initialization. However, as pointed out by Li *et al*. [8], this is not an issue in the LPBF application, as the nominal slice contour information can be used to drive the initialization step. This makes active contours particularly suitable for layerwise image segmentation in LPBF. In particular, we compare two region-based algorithms, i.e., the so-called Active Contours without Edges (ACWE) proposed by Chan and Vese [19] and the more recent level set method with bias field estimation (LSE BFE) proposed by Li *et al*. [20]. Their use in LPBF applications have been advocated by Abdelrahman *et al*. [7] and Li *et al*. [8], respectively, but, to the best of the authors' knowledge, no characterization of their performances has been carried out so far.

The experimental study was performed by means of an LPBF prototype system with an open architecture that allows gathering high-spatial resolution images of the build area and testing different lighting configurations.

Section 2 briefly reviews the state of the art on layerwise image analysis and monitoring in LPBF; Section 3 presents the real case study and the experimental settings; Section 4 describes the proposed methodology; Section 5 presents the achieved results; Section 6 concludes the paper.

2. STATE OF THE ART

In the recent years, various studies investigated in-situ monitoring methods in LPBF based on the layerwise acquisition of powder bed images: they are summarized in Table 1. One stream of research was devoted to the detection of powder bed inhomogeneity, super-elevated regions and uneven patterns that may interfere with the powder recoating system. Kleszczynski *et al*. [11] presented a first seminal study that showed the capability of high-resolution imaging to identify powder bed defects and uneven patterns, although only qualitative analysis were included. Based on the same experimental setup presented by Kleszczynski *et al*. [11], zur Jacobsmühlen *et al*. [12 – 13] proposed a thresholding approach to automatically detect super-elevated edges. A following study [11] proposed a method to combine in-situ imaging with recoating blade vibration measurements. The idea to use layerwise imaging to detect out-of-plane deviations from a smooth surface was further developed by Land *et al*. [21] and Zhang *et al*. [22]. They proposed a monitoring system that combined off-axis cameras with a fringe projector to measure the topography map of both the scanned slice and the un-melted powder surface in each layer. More recently, Imani *et al*. [23 – 24], Gobert *et al*. [25] and Scime and Beuth [26] proposed different methodologies to automatically extract features representative of local surface pattern variations and to identify defects or wrong melting conditions.

Other authors proposed in-situ monitoring methods based on the segmentation of layerwise images. Foster *et al*. [10] showed that by segmenting layerwise images it was possible not only to detect powder contamination and recoating errors, but also to generate a 3D reconstruction of the part geometry. The issues and challenges related to the achievement of an accurate segmentation of these images was clearly discussed by Aminzadeh (2016), who showed that noisy intensity patterns combined with non-uniform smoothness of solidified regions and non-uniform illumination make traditional edge detection and segmentation algorithms poorly effective. To the best of the authors' knowledge, the studies of Aminzadeh [27] and Aminzadeh and Kurfess [9] are the only ones that attempted to determine the accuracy of in-situ image segmentations. This task was accomplished

by comparing the identified contours with a manual segmentation applied to the same images. The segmentation approach proposed by Aminzadeh [27] and Aminzadeh and Kurfess [9] combined histogram-based thresholding with image pre-filtering and morphological operations, but various ad-hoc thresholds and heuristic settings were needed. A different family of image segmentation methods, i.e., active contours, was proposed by Abdelraham *et al*. [7] and Li *et al*. [8]. Abdelraham *et al*. [7] proposed a method to automatically detect surface anomalies in layerwise images related to uneven surface patterns within the laser printed area. The active contours algorithm developed by Li *et al*. [20] was proposed to register the nominal slice contour to in-situ images in a calibration phase. Li *et al*. [8] proposed the active contours methodology for layerwise image segmentation in the framework of a 3D geometrical reconstruction of the part via in-situ images. In this case, the active contours algorithm was used to identify the region of interest consisting of the printed area within the layer, and then a topography map was estimated via fringe projection coupled with stereo imaging within that region. Li *et al*. [8] discussed the enhanced capability of active contours to deal with the various challenges of LPBF layerwise images. In particular, active contours represent a segmentation approach that prevents from defining ad-hoc thresholds and reduces the need for ad-hoc post-segmentation morphological operations. This study is grounded on this category of image segmentation techniques.

Table 1 – Summary of the literature devoted to LPBF process monitoring via layerwise imaging

Reference	Camera type	Spatial resolution	Illumination	Image segmentation
[11 – 13]	Monochrome SVCam-hr29050, SVS-VISTEK GmbH	24 µm/pixel	Directed light + matt reflectors for diffuse lighting	Not applied
[21]	Single-lens reflex camera + fringe projector	Not specified	Structured light	Not applied
[22]	PointGray Flea3 camera + fringe projection	6.8 µm/pixel	Structured light	Not applied
[23 – 24]	36.3-megapixel DSLR camera (Nikon D800E)	Not specified	Bright field directional lighting	Not applied
[26]	1280 x 1024 pixel stock camera of EOS M290	290 µm/pixel	Side directional lighting	Not applied
[25]	36.3-megapixel DSLR camera (Nikon D800E)	50 µm/pixel	Multiple flash modules	Not applied
[10]	36.3-megapixel DSLR camera (Nikon D800E)	50 µm/pixel (lens A), 15 µm/pixel (lens B)	Multiple flash modules	Not specified
[9; 27]	8.8 megapixel camera	7 µm/pixel	Square LED on the ceiling of the chamber	Histogram-based thresholding
[7]	36.3-megapixel DSLR camera (Nikon D800E)	45-88 µm/pixel	Multiple flash modules	Active contours
[8]	Stereo Basler ace-acA2500-14gm cameras (2592 × 1944 pixels) + fringe projection	Not specified	Structured light + side flash modules	Active contours

3. EXPERIMENTAL STUDY

3.1. System configuration

The experimental study was carried out by using an LPBF prototype system developed at the Department of Mechanical Engineering of Politecnico di Milano. The configuration of the system is shown in Fig. 2. The build area is 60 x 60 mm and the scanning system is an IPG YLR-300, a Ytterbium-doped yttrium aluminium garnet (Yb:YAG) laser source, with a maximum power of 250 W and a wavelength of 1060 nm. The system works in slight argon overpressure of 50 mbar. The argon flow direction is perpendicular to the powder recoating direction and the recoater consists of a flexible silicon blade. To acquire the in-situ images, the prototype system is equipped with an integrated 10.55 Mpix IDS UI-5490SE-C-HQ camera (3840 x 2749 Pixel MT9J003STC CMOS sensor with pixel size equal to 1.67 µm and a pixel depth of 8) mounting a 25 mm lens placed as shown in Fig. 2.

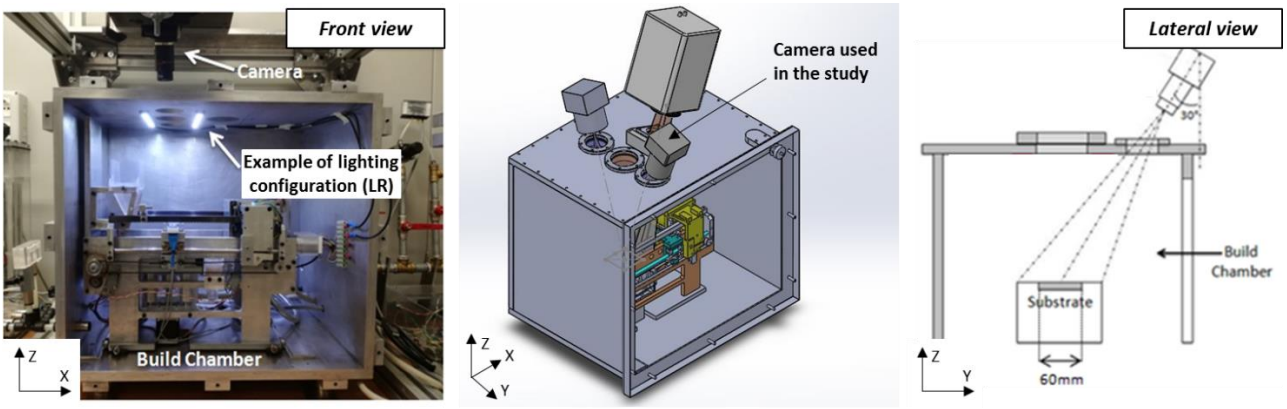

Fig. 2 – Front view (left panel), 3D view (central panel) and later view (right panel) of the PLBF prototype system used for the experimental activity

The imaging system is equipped with six directional light sources consisting of LED strip lights placed in six different locations on the ceiling of the build chamber as shown in Fig. 3. Each light source is labelled with a capital letter: A, B, C, D indicate light sources parallel to the X axis (horizontal light sources), whereas L and R identify the left and right sources parallel to the Y axis (vertical light sources). When multiple light sources are turned on at the same time, e.g., A and L together, the resulting lighting configuration is labelled by the union of capital letters, i.e., AL. The possibility of turning on multiple light sources simultaneously leads to several different combinations of illumination configurations. The light sources were grouped into

four groups: front (A and B), back (C and D), left (L) and right (R). The system configuration allows the generation of dark and bright field illumination patterns [16]. When region (A and B) are turned on, alone or simultaneously to vertical light sources (L and R), a dark field illumination is obtained: the majority of light is not reflected towards the camera. When light sources in the back region (C and D) are turned on, alone or simultaneously to vertical light sources (L and R) a bright field illumination s obtained: the majority of light is reflected towards the camera. When multiple light sources are turned on simultaneously (e.g., double parallel or perpendicular lights, or more than two light sources at a time), other illumination conditions can be generated as well, which do not strictly belong to the two aforementioned conditions. An exhaustive experimentation was carried out in a preliminary stage to investigate the effects of all possible combinations of six available light sources. For sake of space and clarity, a reduced set of 24 lighting configurations is discussed in this study. They are representative of lighting conditions either in industrial LPBF systems or in previous studies (Table 1). As an example, the BCLR configuration is representative of industrial systems equipped with a ring of LED lights around the laser protection glass, whereas single and double parallel light sources are representative of industrial systems equipped with single and multiple directional light sources. Table 2 summarizes all the 24 lighting configurations considered in this study.

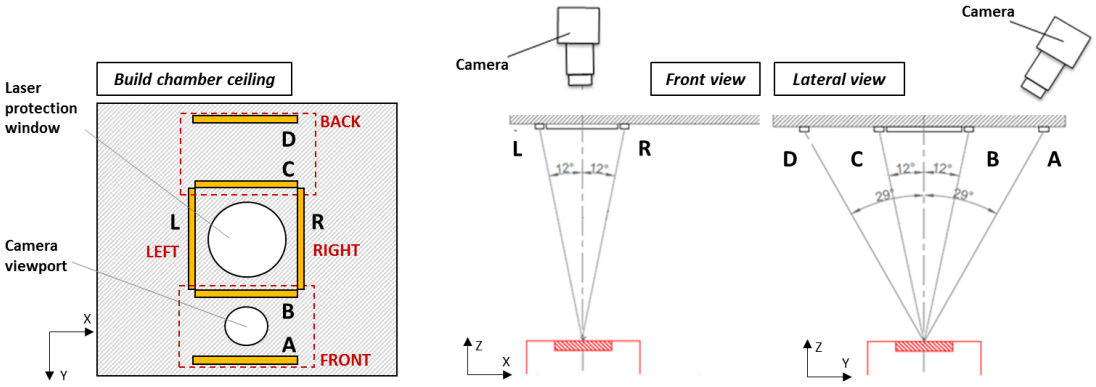

Fig. 3 – Locations of the six directional LED light sources: view of the build chamber ceiling (left panel), front view (central panel) and lateral view (right panel)

A checkerboard calibration of the camera [28] was performed to correct the perspective error and to estimate the actual spatial resolution. In this study, an in-situ spatial resolution of 20 µm/pixel over the entire build area was achieved. All the ex-situ images were acquired by means of a Mitutoyo Quick Vision Active

optical microscopy equipped with a 2.5X lens. The spatial resolution of ex-situ images was one order of magnitude higher than the one available in-situ, i.e., about 1,9 μm/pixel.

Table 2 – List of 24 lighting configurations tested in the presented experimentation

	Dark field							Bright field							Other configurations								
Vertical light	None	None	Left	Right	Left	Right	Both	None	None	Left	Right	Left	Right	Both	Left	Right	None	None	None	None	Both	Left	Right	Both
Horizontal light	Front	Front	Front	Front	Front	Front	Front	Back	Back	Back	Back	Back	Back	Back	None	None	Both	Both	Both	Both	None	Both	Both	Both
ID	A	B	AL	AR	BL	BR	BLR	C	D	CL	CR	DL	DR	CLR	L	R	AC	AD	BC	BD	LR	BCL	BCR	BCLR

3.2. LPBF process and designed experiments

Five different builds were manufactured via LPBF of AISI 316L steel by using the prototype system described in Section 4.1. with fixed default process parameters listed in Table 3. The AISI 316L powder had an average particle size of 25 μm. A summary of builds produced during the experimental activity is shown in Table 4.

Table 3 – Default process parameters used to produce all the specimens

Laser Power	Scan speed	Hatch distance	Scan strategy	Layer thickness
225 W	500 mm/s	0,07 mm	Meander	0,05 mm

Table 4 – Summary of builds included in the experimentation, corresponding experimental plan and goals

	Plan	Purpose
Build 1	Full factorial, 2 factors, 2 replicates Specimen shape (2 levels): cylinders and parallelepipeds Scan direction in top layer (4 levels): 0°, 45°, 90°, 135°	Tuning of segmentation algorithm parameters
Build 2	Replicate of Build 1	Scan direction effect analysis
Build 3	Latin-square, 1 factor, 3 replicates Specimen shape (3 levels): cylinders, parallelepipeds and triangular prisms; Fixed scan direction in top layer: 0°	Lighting condition screening Measurement system performance characterization
Build 4	Replicate of Build 3	
Build 5	Replicate of Build 3 (repeated image acquisition of the same layer)	Measurement system performance characterization Measurement repeatability evaluation

The first two builds, hereafter denoted by Build 1 and Build 2, included 16 specimens: 8 cylindrical specimens of nominal diameter $d = 5\ mm$, and 8 parallelepiped specimens with squared base area of nominal side $l = 5\ mm$. The process was interrupted at the 80th layer, i.e., at height $Z = 4\ mm$ above the build plate and images of the last layer were acquired both in-situ and ex-situ. The scan direction was rotated by 45° at each layer, and the starting scan direction for each specimen was varied such that, in the last layer, the slices were printed with four different scan directions with respect to the X axis, i.e., 0°, 45°, 90° and 135°. Each build was designed such that two replicates of the same scan direction were available in the last layer for each shape, i.e., circles and squares. A random spatial allocation of the specimens on a 4 x 4 regular grid was performed in each build (see Fig. 4, left panel). Build 1 was used for the calibration of the ACWE and LSE BFE algorithms, i.e., for the choice of parameter ϑ in both the methods and the kernel parameter in the LSE BFE method. The selected values of these parameters were then used for all the other experiments. Build 2 was used to investigate whether the scan direction had a statistically significant effect on the segmentation performances for the different lighting conditions.

Fig. 4 shows one example of in-situ image acquired for the last layer of Build 2 (Fig. 4 a), the corresponding ex-situ image (Fig. 4 b) and the ground-truth contours superimposed to the in-situ image (Fig. 4 c). The scan angles applied to produce the last layer of each specimen are shown in Fig. 4 b.

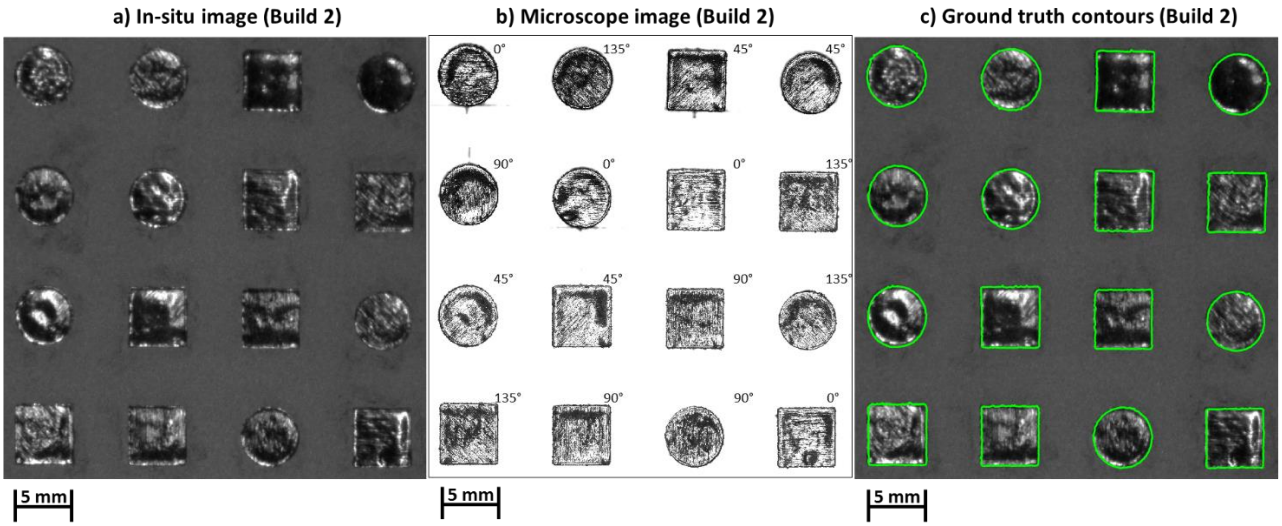

Fig. 4 – Example of in-situ image of Build 2 (a), corresponding ex-situ image (b) and superimposition of ground-truth contours on the original in-situ gathered image (c)

Based on the results of these preliminary analysis, two additional builds, hereafter denoted by Build 3 and Build 4, were manufactured with the same AISI 316L powder and the same process parameters. These builds were used to screen out worst illumination configurations and to perform the measurement system performance characterization study. Build 3 and Build 4 consist of a 3 x 3 latin-square design of three different geometries: three cylindrical specimens of nominal diameter $d = 5\ mm$, three parallelepiped specimens with squared base area of nominal side $l = 5\ mm$, and three isosceles triangular prisms with base of height $h = 6\ mm$ and angles equal to 67.38° and 45.24°. Analogously to the previous two builds, the process was interrupted at the 80th layer, and images of the last layer were acquired both in-situ and ex-situ. Differently from the previous two builds, in Build 3 and Build 4 all the slices belonging to different shapes were printed with the same scan direction in each layer. In the last layer, the scan angle with respect to the X axis was 0° for all the shapes[1]. One additional build, i.e., Build 5, was produced to estimate the measurement repeatability. It is a replicate of Build 3 and 4, but multiple (three) in-situ images of the same layer were acquired under each illumination condition. Fig. 5 shows two examples of in-situ images acquired for the last layer of Build 3 (Fig. 5 a) and Build 4 (Fig. 5 d), the corresponding ex-situ images (Fig. 5 b and Fig. 5 e) and the ground-truth contours superimposed to the in-situ images (Fig. 5 c and Fig. 5 f).

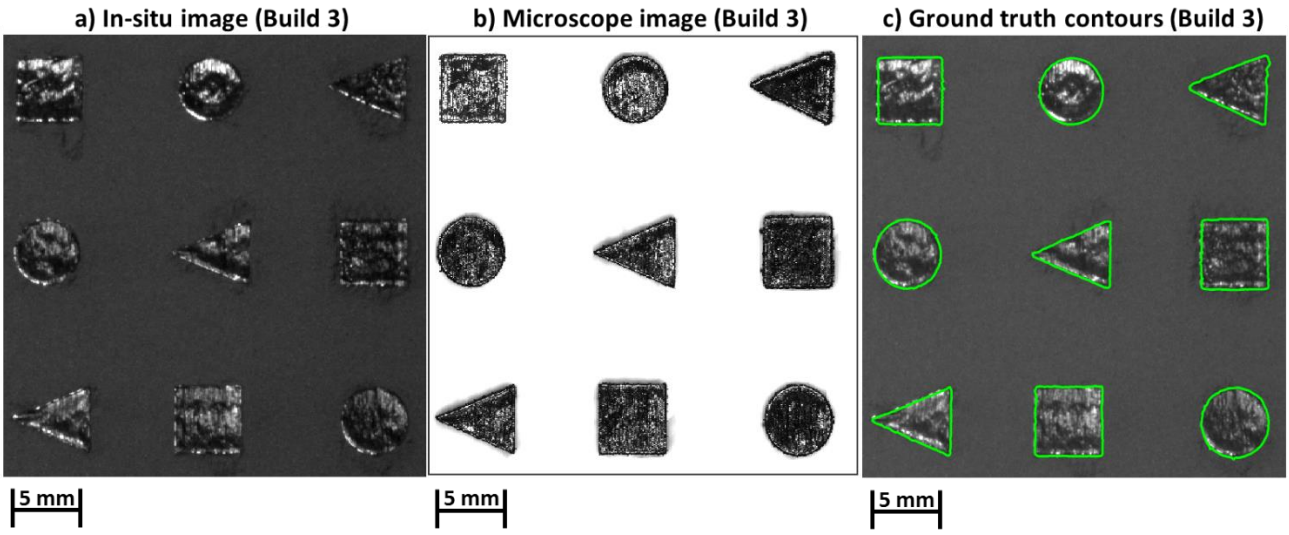

Fig. 5 – Example of in-situ image of Build 3 (a), corresponding ex-situ image (b) and superimposition of ground-truth contours on the original in-situ gathered image (c)

[1] Indeed, the results discussed in Section 5 show that the scan direction had no statistically significant effect on the segmentation performances.

4. METHODOLOGY

The active contours methodology has been applied to static image segmentation of single images and boundary tracking in temporal image sequences since the first introduction of so-called "snakes" by Kass *et al*. [29]. The underlying idea consists of implementing an iterative method that starts with a first boundary definition in the form of a closed curve. Then, the shape of this boundary is iteratively changed and adapted by applying shrink/expansion operations called "contour evolution" driven by the minimization of an energy function. Active contour methods can be divided in two classes: edge-based and region-based [17 – 18]. Edge-based methods work by finding discontinuities in the intensity of an image, where an edge consists of a boundary between two regions characterized by different properties (e.g., pixel intensities). They rely on local derivative estimation, and hence they are not very effective in the presence of weak object boundary and noisy patterns like in layerwise images in LPBF. Abdelraham *et al*. [7] and Li *et al*. [8], proposed the use of a region-based active contour technique, which exploits a certain region descriptor to guide the contour evolution. The algorithm works by segmenting the image so that each region has homogeneous properties. Active contours are more robust than edge-detection based techniques with respect to image noise and not well-defined edges, but they can perform poorly if the foreground region has non-homogeneous intensity, which strongly depends on lighting conditions [17; 20]. The ACWE method proposed by Chan and Vese [19] and applied by Li *et al*. [8] to LPBF images is a well-known approach belonging to this category. In the presence of heterogeneous foreground, the ACWE method, like other analogous region-based methodologies may be not effective in identifying both the dark and bright areas of the foreground region. The LSE BFE method proposed by Li *et al*. [20] and implemented by Abdelraham *et al*. [7] is instead specifically aimed at overcoming this limit, but at the expense of an increased algorithm complexity and longer computational time. The LSE BFE method belongs to the region-based active contour category, but it is able to segment regions characterized by non-homogeneous intensity. This is achieved by introducing a local clustering criterion for intensities in a neighbourhood of each pixel.

The ACWE and LSE BFE methodologies are briefly reviewed in Appendix A. Section 4.1 presents the proposed approach to apply these methods to layerwise image segmentation in LPBF; Section 4.2 describes the proposed methodology to evaluate the image segmentation and to determine the accuracy and repeatability of dimensional measurements based on in-situ image segmentation.

4.1. Layerwise image segmentation

The active contours methodology implementation requires the definition of the initial contour, i.e., the zero-level set function to initialize the iterative segmentation procedure. To this aim, an approach similar to the ones used by Abdelraham *et al*. [7] and Li *et al*. [8]. The underlying idea consists of exploiting the knowledge of the region of interest corresponding to the nominal slice contour in each layer. More specifically, we defined the initial level set function as the bounding box of the nominal contour available from the sliced model of the part.

We also investigated the possibility to enhance the segmentation capability by pre-processing the in-situ gathered images. Indeed, both active contours methods reviewed in Appendix A rely on the assumption that the two regions have different mean intensities. However, as shown in Fig. 6 (top panels), because of the inhomogeneous intensity within the printed region caused by an uneven surface pattern, the foreground area exhibits intensity values spread over an interval that is overlapped with respect to background intensities. It is known from the literature [17 – 18] that when foreground regions include both darker and brighter areas than the background, the traditional active contours algorithm tends to segment either the dark or bright zones. Because of this, two implementations of the ACWE and LSE BFE algorithms were considered. The first consists of the direct application of the two algorithms to the original images. The second involves a pre-processing step aimed at increasing the gap between average foreground and background intensities. The proposed pre-processing operation consists of transforming the post-scan image by subtracting the average background intensity estimated from pre-scan images, and then applying the absolute value to the resulting difference of pixel intensities. This yields the following transformation of the original image:

$$U_0(x,y)^* = abs(U_0(x,y) - \overline{U}_{0,pre}) \tag{1}$$

where x and y are the pixel coordinates, $U_0(x,y)^*$ is the transformed pixel intensity and $\overline{U}_{0,pre}$ is the average pixel intensity of the image captured before the laser scanning. This transformation allows converting the portions of the foreground region that are darker than the loose powder intensity into brighter ones. Fig. 6 (bottom panels) shows that this pre-processing operation enlarges the gap between foreground and background intensities and it also reduces the pixel intensity variability within the foreground area. In the remaining of the

paper, the nomenclature “transformed image” is used to highlight when either the ACWE or the LSE BFE algorithms were applied to images pre-processed via expression (1).

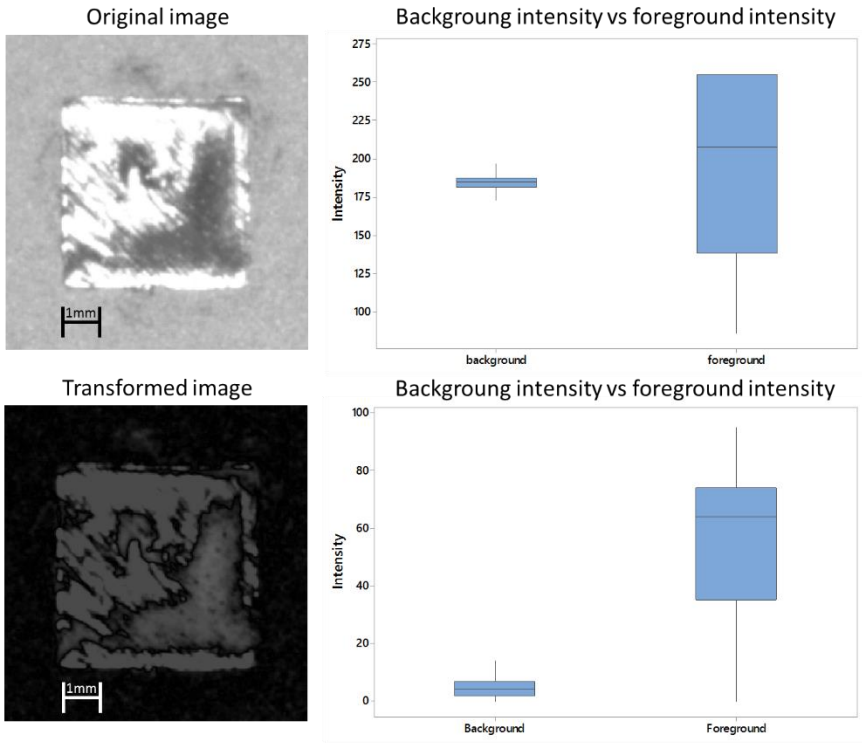

Fig. 6 – Example of original (top-left panel) and transformed (bottom-left panel) image with the corresponding pixel intensity boxplots (right panels) of foreground and background regions

4.2. Characterization of in-situ measurement

In order to characterize the performances of in-situ measurements we compared them against a reference, also known as measurement standard in metrology or ground-truth in the machine vision literature [30; 16], defined on the basis of ex-situ optical microscopy images of the additively produced specimens. The following procedure was applied.

1. The LPBF process of the simple geometrical features mentioned in Section 3 was interrupted after a pre-defined number of layers (no top-skin scanning was performed while producing the last layer);
2. A sufficient time was waited before acquiring in-situ images to let the parts cool down to room temperature, in order to capture images representative of the actual dimensions and shape after the shrinkage;

3. In-situ high-resolution images were acquired before and after the laser scan in the last layer;
4. The part was removed from the system and ex-situ optical microscopy images of the top layer were acquired.

The comparison between in-situ and ex-situ measurements was performed in two sequential steps. First, a simple image segmentation evaluation criterion [30] was used. It consists of a pixel-wise and non-shape dependent comparison between the in-situ and ex-situ foreground regions, which was suitable to preliminarily to screen out lighting conditions that yielded poor segmentation results, but also to assess the possible effect of the scan direction and to calibrate the active contours algorithms (i.e., to select the parameter values to be used in the energy functional minimization problem). Then, the measurement system performance characterization was performed to determine the measurement accuracy in the presence of best segmentation conditions only, by estimating the dimensional measurement error of specific benchmark geometrical features.

Regarding the preliminary image segmentation evaluation step, several criteria are available in the literature [30]. The more consolidated approach relies on the comparison with a so-called ground-truth reference that represents the correct segmentation for the current image. This involves computing a measure of similarity (or dissimilarity). In this study, we refer to the Dice's index [31 – 32], a region-based similarity index extensively used in image analysis. Differently from [9], where the ground-truth was determined by manually segmenting the in-situ images, the use of ex-situ images was motivated by the need of a ground-truth definition with a resolution of an order of magnitude higher. In particular, ex-situ images were segmented by combining image pre-processing and a human-assisted iterative refining of active contours-based segmentation. The Dice's index is defined as follows [31]. Let Ω_{insitu} and Ω_{truth} be, respectively, the foreground regions identified from in-situ image segmentation and the corresponding ground-truth reference after registration. The Dice's metric computes the intersection area between Ω_{insitu} and Ω_{truth} normalized with respect to the mean sum of individual areas. It is defined as follows:

$$Dice(\Omega_{insitu}, \Omega_{truth}) = \frac{2\|\Omega_{insitu} \cap \Omega_{truth}\|}{\|\Omega_{insitu}\| + \|\Omega_{truth}\|} \quad (2)$$

where ‖·‖ represents the number of pixels in the region. The index ranges between 0 and 1, where 1 means that the two regions coincide, whereas 0 means that there is no intersection between the regions. The Dice's index estimation requires a registration between the ground-truth contours and the in-situ images. To this aim, a landmark registration involving a non-reflective similarity transformation (i.e., rigid translation, rotation and resampling with no reflection) was applied to couples of in-situ and ex-situ images, before applying any segmentation algorithm [33]. The landmarks were manually selected in both in-situ and ex-situ images, corresponding to the four corners of the build. The registration transformation was estimated once for each build and applied to images acquired under every lighting conditions.

Once the algorithms have been calibrated and only lighting conditions that provided the highest quality segmentations (i.e., highest Dice's index values) were retained, the dimensional error was estimated by means of a robust minimum squared error fitting of identified contours for the measurement of different geometrical features, including the diameter of circular shapes, the side length of squared shapes and the angles of triangular shapes.

Fig. 7 shows the geometrical features whose dimensions were measured by means of both in-situ and ex-situ images. The sides of squared shapes were labelled as l_x and l_y, the diameter of circular shapes was denoted as d, whereas the angle at the apex of the isosceles triangles was denoted as β.

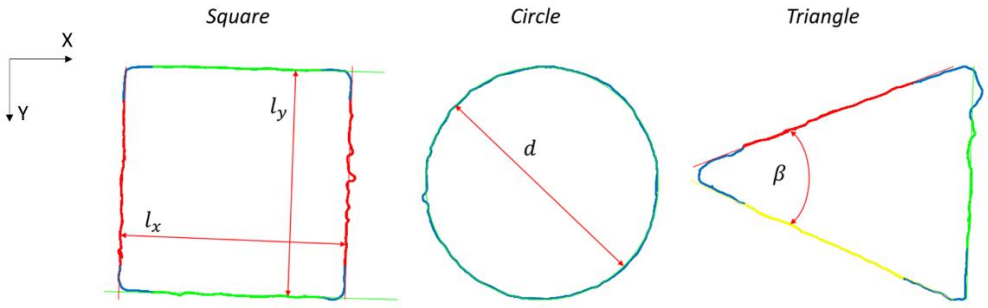

Fig. 7 – Example of simple geometrical features measured by means of the robust minimum squared error fitting approach

Once the images had been converted into a point profile via image segmentation, the linear sizes considered (circle diameter and side of the squared shape) were defined and estimated in accordance to the ISO 14405-1

standard [34]. A global least squares size has been considered. In the case of the side of the square, this requires the solution of the following problem:

$$\min_{a,b,c_1,c_2}\left(\sum_{i=1}^{n_1}\left(\frac{ax_{i,1}+by_{i,1}+c_1}{\sqrt{a^2+b^2}}\right)^2+\sum_{j=1}^{n_2}\left(\frac{ax_{j,2}+by_{j,2}+c_2}{\sqrt{a^2+b^2}}\right)^2\right) \tag{3}$$

where a, b, c_1, c_2 are optimization parameters, n_1 is the number of points identified in one side, $(x_{i,1}, y_{i,1})$ are the coordinates of the i[th] point of this side, and similarly n_2 is the number of points identified in the opposite side and $(x_{j,2}, y_{j,2})$ are the coordinates of the j[th] point. The side is then given by $|c_1 - c_2|/\sqrt{a^2+b^2}$. In the case of the diameter of the circumference, the following problem must be solved:

$$\min_{d,x,y}\left(\sum_{i}^{n}\left(\sqrt{(x_i-x)^2+(y_i-y)^2}-\frac{d}{2}\right)^2\right) \tag{4}$$

where d, x, y are optimization parameters, n is the number of points identified on the circumference, and (x_i, y_i) are the coordinates of the i[th] point. The diameter is then given by d.

The apex angle was defined, in accordance with the ISO 14405-3 standard [35], as a two-line prismatic angular size, the two sides being independently fitted by least squares. The two sides where independently fitted by solving:

$$\min_{a,b,c}\left(\sum_{i=1}^{n}\left(\frac{ax_i+by_i+c}{\sqrt{a^2+b^2}}\right)^2\right) \tag{5}$$

where a, b, c are optimization parameters, n is the number of points identified one of the sides, and (x_i, y_i) are the coordinates of the i[th] point. Once the sides have been fitted, as the parameters a, b con be geometrically interpreted as normal to the direction vector of the line, the apex angle can be easily obtained.

In all cases the outlying points where iteratively discarded to obtain a robust fitting. In the case of the triangle and of the square shape the points close to the vertices where discarded, as it was difficult to attribute them to one or the other side.

It is worth noting that the final dimensional error characterization does not require any registration between in-situ and ex-situ images. Therefore, if registration inaccuracy exists, it may produce a constant bias in the Dice's index computation but not in the final dimensional error estimation.

The characterization of the layerwise image-based dimensional measurement involves the analysis of the sources of variability that affect the measurement. Generally speaking, this kind of analysis, also known as gauge repeatability and reproducibility (R&R) study, entails a decomposition of the total variability, σ_{tot}^2, into the variability due to different parts, the variability due to different operators, and the variability due to the gauge itself [36]. In our study, the measurement system is not operator-dependent, as the camera is fixed and all calibration and image segmentation operations can be automated. Therefore, the sources of variability consist of part-to-part variability, σ_{part}^2, build-to-build variability, σ_{build}^2, and pure error, σ^2. The part-to-part and the build-to-build variability represent the variability in the measurement result that is not due to measurement errors, but to the fact that more than one build has been manufactured, and more than one part per build has been executed. The part/builds are not exactly identical, indeed. The pure error instead considers the variability due to the difference of repeated measurements of a single build. As all the measurements were conducted exactly in the same conditions, and all the algorithms adopted for the image analysis were deterministic, this variability is due to uncontrollable effects like, as an example, the reading noise of the sensor. As such, it is an estimate of the measurement repeatability. A random effect model was used to decompose the total measurement variability into these terms. For each measured quantity, i.e., side lengths of squared shapes, diameter of circular shapes and angle at the apex of triangular shapes, a two-factor random effect model [36] was fitted to data gathered by producing Build 3, 4 and 5. The response variable was the measurement result, and design factors are the builds and the parts within the builds. The factor "part" was nested into the factor "build" leading to the following random effect model:

$$y_{ijk} = \mu + \tau_i + \beta_{j(i)} + \epsilon_{ijk} \tag{6}$$

where $i = 1, \dots, 3$ (number of builds), $j = 1, \dots, 3$ (number of parts of the same shape in each build), and $k = 1, \dots, n_i$ (number of measurement repetitions in the i-th build). μ is the the mean dimension measured in-situ, and hence $\mu - \mu_{ref}$ (where μ_{ref} is the corresponding mean dimension measured ex-situ) represents the estimate of the measurement bias. The measurement bias is the systematic measurement error committed every time a part is measured. Even if, once the bias has been estimated, it can be corrected, in general measurement characterized by a small bias are preferable, as bias estimate can be difficult and expensive. τ_i indicates the build factor, whereas $\beta_{j(i)}$ indicates the part factor, where the subscript $j(i)$ indicates that the part factor is nested into the build factor. ϵ_{ijk} is the random error term.

Based on the model (6), the following decomposition of the total measurement variability was obtained:

$$\sigma_{tot}^2 = \sigma_{part}^2 + \sigma_{build}^2 + \sigma^2 \quad (7)$$

Indeed, the error variability, σ^2, in our nested design coincides with the pure error variability associated to the repeated measurements in Build 5, and hence it was used as an estimate of the measurement repeatability.

5. RESULTS

5.1. Preliminary analysis

The results of the analysis aimed at selecting the value of the penalization coefficients in both ACWE and LSE BFE algorithms, and the kernel parameter in the LSE BFE algorithm are detailed in Appendix B. They showed that both the active contours methodologies are robust to the choice of the penalization coefficients, whereas the kernel width has a significant effect on the segmentation performances of the LSE BFE algorithm. In all the analysis presented in this study, the LSE BFE performances were always evaluated based on the corresponding optimal value of the kernel width parameter based on Build 1 data. All other penalization coefficients involved in both ACWE and LSE BFE algorithms were kept fixed.

The effect of the laser scan direction was investigated by means of a two-way (shape and scan direction) Analysis of Variance (ANOVA) applied to the Dice's similarity index provided by four different methods: ACWE on original images, ACWE on transformed images, LSE BFE on original images and LSE BFE on

transformed images. The ANOVA results (see Appendix C) revealed that for none of the considered lighting conditions neither the shape nor the scan direction were statistically significant at familywise confidence of 5%, with the only exception of lighting configurations AD and BD for which the scan angle resulted to have a significant effect. Both configuration AD and BD combined two horizontal light sources parallel to the X axis, and they yielded a significantly lower segmentation performance in the presence of scan angle 90°, i.e., when the direction of scanned hatches was perpendicular to the LED strips direction. Indeed, under these conditions, the surface pattern irregularity associated to the scanned hatches was emphasized and resulted in worst segmentation results caused by a stronger inhomogeneity of pixel intensities within the foreground region.

These results highlight that the two active contours methodologies are quite robust with respect to the scanning direction for almost all the lighting conditions, and especially for the lighting conditions that provided the best segmentation performances. Because of this, the following analysis were performed fixing the scan angle at 0° value.

5.2. Effect of illumination conditions

The results of the preliminary screening of lighting conditions are displayed in Table 5. Table 5 shows the sample mean and the sample standard deviation of Dice's index values for the compared methods in each lighting configuration. Fig. 8 shows the 95% confidence intervals for the Dice's index provided by the ACWE and LSE BFE methodologies when they were applied either to the original or transformed images.

Table 5 and Fig. 8 (left panels) show that when the image segmentation was applied to the original images only the dark field configuration consisting of the single light source A (one horizontal light source in the front region and no vertical light source) yielded a high segmentation performance, significantly higher than all other configurations. When the segmentation algorithms were applied to the transformed images, instead, there was a considerable improvement of the segmentation performances for various lighting configurations (Fig. 8, right panels). They include all the configurations where at least one front horizontal light source was present, either alone (i.e., A and B) or together with vertical light sources (i.e., AL, AR, BL, BR, BLR). All these configurations belong to the dark field condition, whose benefit consists of yielding a smoother pixel intensity pattern within the foreground region, which finally improved the segmentation. Fig. 8 (right panels) shows

that good segmentation was also achieved in the presence of configurations combining both front and back horizontal light sources in addition to one or both vertical light sources (i.e., BCL, BCR, BCLR), especially when the ACWE method was applied. In this case, the pre-processing operation defined in expression (1) combined with multi-source lighting yielded a quite smooth intensity pattern within the foreground region, that finally led to a more accurate contour identification with respect to the one achieved by segmenting the original images.

Table 5 – Mean Dice's index and standard deviation (in brackets) for different segmentation methods in the presence of all the lighting conditions

	Vertical	Horizont	ID	Dice's index			
				LSE BFE		ACWE	
				Original image	Transformed image	Original image	Transform. image
Dark field	None	Front	A	**0.938 (0.029)**	**0.951 (0.073)**	**0.927 (0.0589)**	**0.962 (0.017)**
	None	Front	B	0.870 (0.142)	**0.950 (0.039)**	0.827 (0.213)	**0.955 (0.017)**
	Left	Front	AL	0.748 (0.140)	**0.942 (0.034)**	0.670 (0.236)	**0.948 (0.020)**
	Right	Front	AR	0.794 (0.120)	**0.912 (0.047)**	0.728 (0.142)	**0.937 (0.033)**
	Left	Front	BL	0.734 (0.145)	**0.938 (0.028)**	0.696 (0.193)	**0.945 (0.019)**
	Right	Front	BR	0.764 (0.139)	**0.912 (0.060)**	0.733 (0.157)	**0.912 (0.065)**
	Both	Front	BLR	0.787 (0.157)	**0.912 (0.051)**	0.657 (0.131)	**0.937 (0.028)**
Bright field	None	Back	C	0.607 (0.142)	0.911 (0.046)	0.574 (0.149)	0.576 (0.153)
	None	Back	D	0.604 (0.142)	0.868 (0.070)	0.484 (0.157)	0.646 (0.199)
	Left	Back	CL	0.703 (0.143)	0.625 (0.160)	0.575 (0.158)	0.658 (0.151)
	Right	Back	CR	0.696 (0.151)	0.666 (0.156)	0.544 (0.147)	0.683 (0.152)
	Left	Back	DL	0.812 (0.120)	0.809 (0.119)	0.743 (0.187)	0.833 (0.100)
	Right	Back	DR	0.844 (0.108)	0.879 (0.076)	0.788 (0.143)	0.796 (0.159)
	Both	Back	CLR	0.762 (0.126)	0.863 (0.087)	0.661 (0.116)	**0.888 (0.083)**
Other configurations	Left	Both	BCL	0.721 (0.174)	**0.879 (0.092)**	0.676 (0.121)	**0.936 (0.023)**
	Right	Both	BCR	0.763 (0.147)	**0.914 (0.040)**	0.623 (0.139)	**0.919 (0.033)**
	Both	Both	BCLR	0.791 (0.122)	**0.922 (0.067)**	0.663 (0.194)	**0.945 (0.023)**
	None	Both	AC	0.658 (0.166)	0.703 (0.226)	0.560 (0.154)	0.813 (0.162)
	None	Both	AD	0.664 (0.099)	0.713 (0.190)	0.518 (0.162)	0.691 (0.225)
	None	Both	BC	0.700 (0.194)	0.866 (0.091)	0.611 (0.115)	0.885 (0.075)
	None	Both	BD	0.764 (0.111)	0.797 (0.197)	0.587 (0.170)	0.817 (0.167)
	Left	None	L	0.626 (0.155)	0.822 (0.156)	0.449 (0.143)	0.852 (0.145)
	Right	None	R	0.721 (0.181)	0.863 (0.111)	0.606 (0.250)	0.876 (0.108)
	Both	None	LR	0.710 (0.143)	0.863 (0.097)	0.590 (0.106)	**0.896 (0.052)**

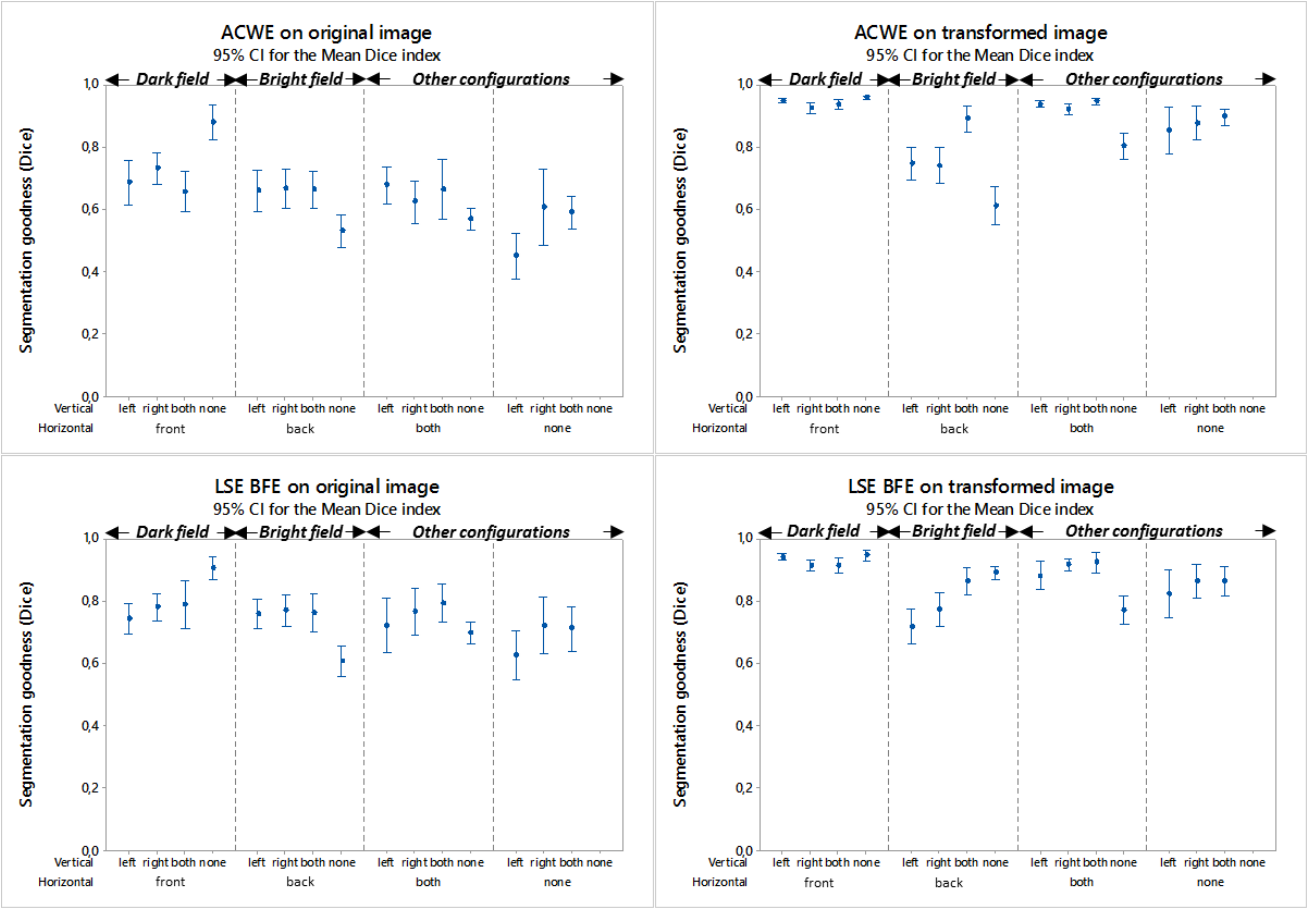

Fig. 8 – 95% confidence intervals for the mean Dice's index for the following methods: ACWE on original images (top-left panel), ACWE on transformed image (top-right panel), LSE BFE on original images (bottom-left panel), LSE BFE on transformed image (bottom-right panel)

According to a Tukey's multiple comparison test at 95% confidence level [36], when both the ACWE and LSE BFE algorithms were applied to original images, the single light source A yielded segmentation performances significantly higher than all the other lighting configurations. When the ACWE algorithm was applied to transformed images, 12 lighting configurations (highlighted with bold fonts in Table 5) resulted to yield Dice's index values that were statistically higher than all other conditions and not statistically different from each other. When the LSE BFE algorithm was applied to transformed images, this was achieved in the presence of 10 lighting configurations (highlighted with bold fonts in Table 5). In practice, the pre-processing operation (1) makes the segmentation performances more robust to illumination thanks to the enhanced gap between foreground and background intensities, and this allowed achieving quite good results for several different configurations.

For sake of space, in the following measurement system performance characterization, only illumination conditions corresponding to an average Dice's index larger than 0.95 were considered. According to Table 5, this leads to configuration A for the segmentation algorithms applied to original images, and configurations A and B when the segmentation algorithms were applied to the transformed images. It is worth mentioning that, in most the cases, the triangular shapes yielded worse Dice's index values than other shapes. This issue was further investigated in the measurement performance characterization discussed in sub-section 5.3.

5.3. Measurement system performance characterization

Table 6 shows the sources of variability for the compared methods in the presence of the most suitable illumination conditions discussed in sub-section 5.2. The results refer to four measured quantities, i.e., the side of squared shapes along the X and Y axis, l_x and l_y, the diameter of circular shapes, d, and the angle at the apex of the isosceles triangles, β. Fig. 9 shows the 95% confidence intervals for the mean dimensional errors superimposed to all the individual measurement errors.

In different cases, the build-to-build variability was approximately equal to zero. This regards conditions where the difference among the builds was strongly non-statistically significant, and hence the build-to-build variability contribution to the total variability decomposition was negligible.

In addition to the variability source decomposition, the bias between in-situ and ex-situ sample mean dimensional measurements is shown in the last column of Table 6. Table 6 shows that all the segmentation methods applied either to original or transformed images are characterized by a quite low pure error, i.e., a quite high measurement repeatability. As an example, $\sigma < 40\ \mu m$ for l_y, l_x and d (i.e., less than 0.8% of the reference dimension), and $\sigma = 1° - 4°$ for β (i.e., less than 9% of the reference dimension). The highest repeatability for all measured quantities was yielded by the LSE BFE method applied to original images (lighting condition A). In that case, the repeatability reduced to $\sigma < 5.7\ \mu m$ for l_y, l_x and d (i.e., less than 0.1% of the reference dimension), and $\sigma = 0.6°$ for β (i.e., about 1.3% of the reference dimension).

Table 6 – Measurement variability sources and measurement bias for different: image pre-processing approach (1), illumination condition (2), segmentation method (3), and measured quantity (4)

(1)	(2)	(3)	(4)	Total var. σ_{tot}	Pure error σ	Build-to-build σ_{build}	Part-to-part σ_{part}	Bias
Original image	A	ACWE	l_y [µm]	80.19	11.71	56.22	55.97	-329.88
			l_x [µm]	54.09	5.37	~ 0	53.82	-32.54
			d [µm]	161.03	5.70	~ 0	160.93	-113.13
			β [°]	8.05	3.51	~ 0	7.25	-3.29
		LSE BFE	l_y [µm]	78.92	5.44	62.85	47.43	-328.93
			l_x [µm]	57.41	3.67	~ 0	57.29	-48.15
			d [µm]	142.68	5.68	~ 0	142.57	-128.40
			β [°]	5.38	0.55	0.62	5.31	-4.20
Transformed image	A	ACWE	l_y [µm]	102.97	8.00	0.00	102.66	-185.33
			l_x [µm]	109.89	12.51	68.01	85.41	-122.402
			d [µm]	128.26	39.09	~ 0	122.16	-171.56
			β [°]	3.72	1.23	~ 0	3.51	-2.20
		LSE BFE	l_y [µm]	105.90	8.10	~ 0	105.59	-148.00
			l_x [µm]	85.63	12.67	~ 0	84.69	-84.94
			d [µm]	129.41	39.59	~ 0	123.21	-134.83
			β [°]	4.32	1.53	~ 0	4.04	-3.00
	B	ACWE	l_y [µm]	97.09	8.81	62.77	73.55	-159.64
			l_x [µm]	84.75	22.43	57.08	58.49	-106.10
			d [µm]	122.82	23.89	~ 0	120.48	-160.36
			β [°]	2.42	1.64	~ 0	1.78	-2.14
		LSE BFE	l_y [µm]	133.23	8.92	109.39	75.53	-121.97
			l_x [µm]	63.26	22.72	~ 0	59.04	-64.17
			d [µm]	128.29	24.20	33.74	121.39	-124.12
			β [°]	1.93	1.05	~ 0	1.62	-2.40

All the considered methods were quite comparable in terms of build-to-build, part-to-part and total variability: this denotes that the repeatability of the measurement is small compared to the part-to-part variability. The only exception is the measurement of the angle β based on the ACWE method applied to the original images. This was caused by a higher variability in the identification of slice contours corresponding to the corners of the triangular shapes, which have a relevant impact on the corresponding measurement repeatability. In all cases, the pure error is up to one order of magnitude lower than the total variability: most of the variability depends then on the natural variability of the process, and not on the measuring instrument. As such the precision of the system in the identification of the dimension characteristics should be considered adequate to monitor the process: if there is a significant deviation from the nominal behaviour, the measuring system, together with an adequate image processing and segmentation method, will be able to identify it.

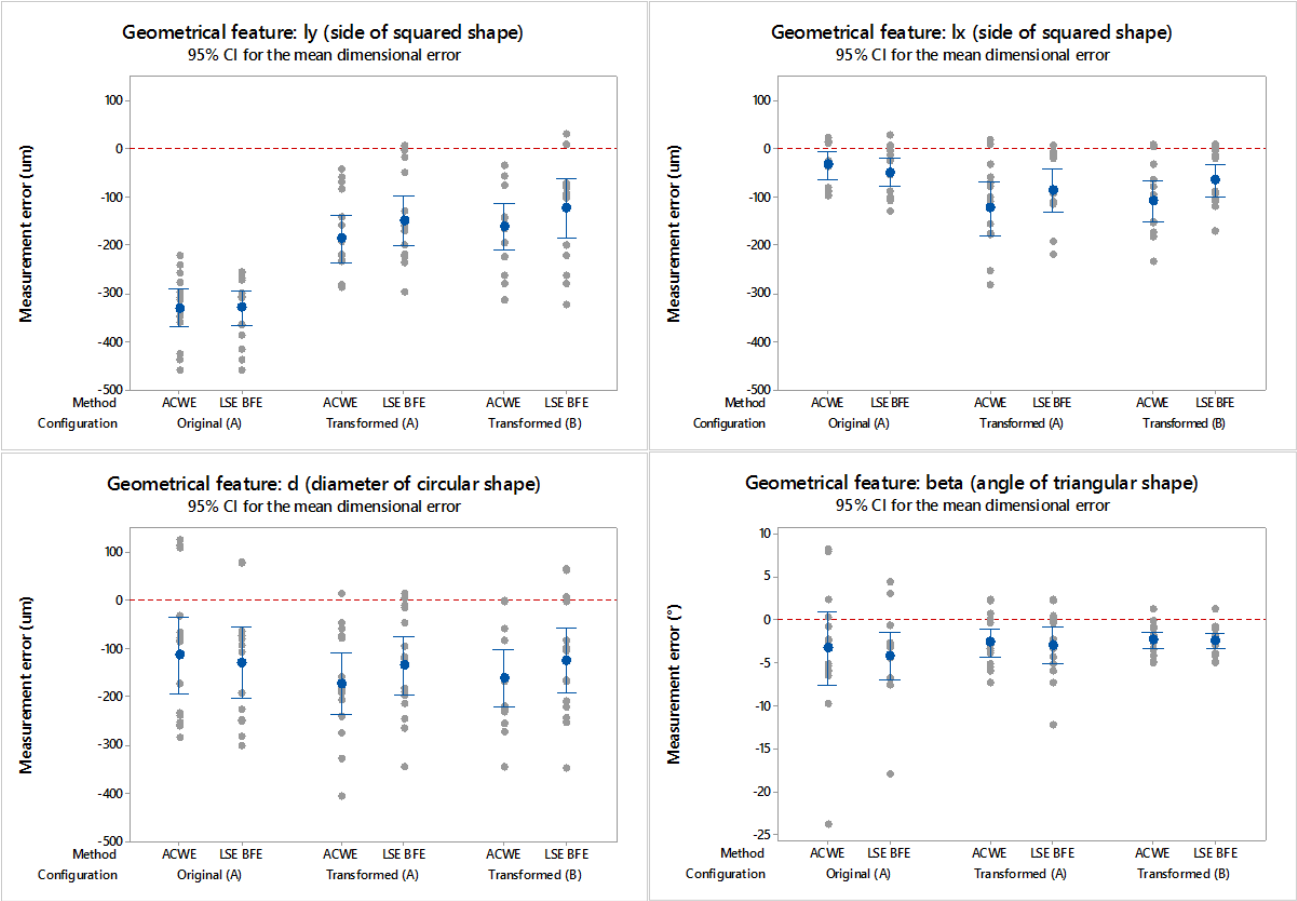

Fig. 9 – Individual measurement errors and 95% confidence intervals of mean measurement errors for the following measured quantities: l_y (top-left panel) l_x (top-right panel), d (bottom-left panel) and β (bottom-right panel)

Fig. 9 shows that in-situ measurements tend to underestimate all the dimensional quantities: this is expected to be caused by a limited accuracy in the system calibration (a magnification error is present because of the error in the estimation of the pixel size, i.e. the pixel to micrometre conversion) that generates a systematic underestimation in the measurement result. Furthermore, a scale error (the system behaves differently in the *x* and *y* directions) is present: the bias affecting the measurement of l_x is lower than the one affecting the measurement of l_y. The scale error is expected to be due to the camera orientation (Fig. 9). The calibration of the camera needs then an improvement, which can be based on this experimental evidence as well.

In addition to this, there are other effects influencing the measurement bias of l_y. As an example, Fig. 10 shows that both the ACWE and LSE BFE methods applied to original images yielded a much higher bias for

the measurement of l_y than other methods applied to the same images. This was caused by an underestimation of the foreground region produced as shown in Fig. 10. Fig. 10 compares the segmentation of a squared shapes produced by the ACWE method applied to the original image (left panel) and to the transformed image (right panel). For sake of clarity, in both the panels of Fig. 10, the identified contours are superimposed to the original image. Fig. 10 shows that the bottom edge of the shape appears brighter than the rest of the foreground region, because of how the directional light is reflected back to the camera. When the segmentation was applied to the original image, that brighter region was not included into the identified foreground region. The image pre-processing operation (1) allowed the segmentation algorithm to properly include the brighter edge into the segmented region instead, which reduced the error in the estimation of the l_y dimension.

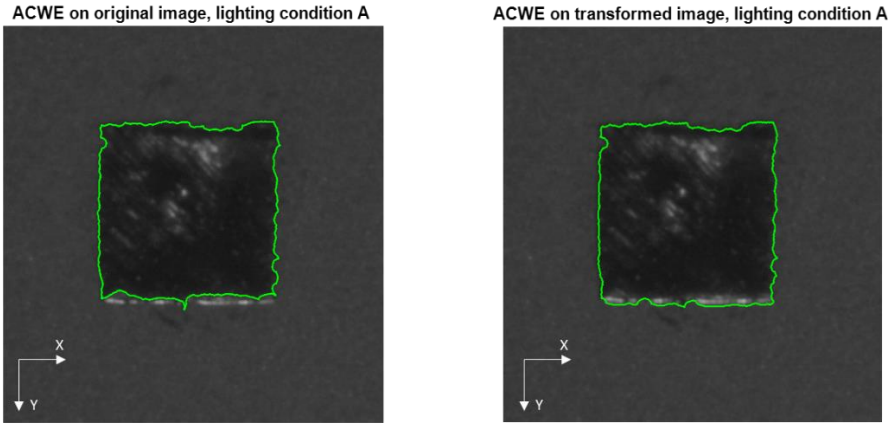

Fig. 10 – Example of in-situ image segmentation for a squared shape in Build 3 obtained by applying the ACWE method to the original image (left panel) and to the transformed image (right panel) in the presence of lighting condition A

The segmentation of images transformed according to expression (1) allows enhancing the measurement trueness in specific cases like the one depicted in Fig. 10, but the segmentation of original images provided a slightly better precision. In both the cases, the irregularity of the contours shown in Fig. 10 was caused by a limited sharpness of edges between the foreground and background regions. The lack of well defined edges was one of the motivating factors for the use of active contours, since it makes poorly effective conventional edge detection and image segmentation techniques [9; 27]. However, future research will be aimed at further improving the quality of the layerwise images working on the image system configuration and on pre-processing operations.

Generally speaking, the ACWE and the LSE BFE methodologies produced analogous measurement performances, although the ACWE involves a simpler and more computationally efficient algorithm than the LSE BFE, which also does not require the estimation of kernel parameters. A further comparison in terms of computational efficiency is discussed in sub-section 5.4.

As pointed out in the introduction, part dimensions measured in-situ are not representative of the final dimensions of the as-built part, as shrinkage effects and thermal stress-induced distortions cannot be captured on a layer-by-layer basis. However, the measurement repeatability and uncertainty discussed above are compatible with the capability of detecting a major deviation from the expected shape, together with the detectability of powder recoating errors. This can be achieved by combining a suitable lighting configuration with active contours image segmentation.

5.4. Computational cost

The computational efficiency of the ACWE and LSE BFE algorithms was estimated on a workstation equipped with an Intel® Xeon® CPU E5-2650 v2 @ 2.60 GHz. Two Matlab® implementations of the algorithms were used in this paper, i.e., the ACWE v.1.0 developed by Dongcai[2] and the LSE BFE toolbox v.1.0 developed by Li[3]. Fig. 11 shows the average percentage contour variation between the i-th and (i-1)-th iteration steps for the measurement configurations considered in Section 5.3, whereas Fig. 12 shows the 95% confidence intervals for the mean duration of one algorithm iteration in the same measurement configurations.

Fig. 11 shows that both the algorithms converge to the final contour identification in very few steps, i.e., less than 10 iterations. However, the ACWE is much more efficient than the LSE BFE, as the average duration of one ACWE iteration is lower than 0.1 s and the average duration of one LSE BFE iteration is larger than 2.8 s. Moreover, the computational cost of the LSE BFE depends on the type of image (i.e., original or transformed) and on the illumination condition. This is mainly driven by the optimal kernel width used in each specific condition. As shown in Appendix B, the segmentation of transformed images requires higher values of the kernel width, which inflates the computational effort, as the K-means clustering is performed on larger

[2] https://it.mathworks.com/matlabcentral/fileexchange/34548-active-contour-without-edge (last access: 18/07/2018)
[3] https://it.mathworks.com/matlabcentral/fileexchange/59752-mri-segmentation-and-bias-field-correction (last access: 18/07/2018)

areas. Considering that both the methods converge in less than 10 iterations for the images considered in this study, the ACWE algorithm requires less than 1 s to provide a measurement, whereas the LSE BFE may require up to 50 s. Being comparable the measurement performances resulting from the implementation of both the methods, the ACWE methodology is more attracting from an in-situ monitoring viewpoint thanks to its enhanced computational efficiency.

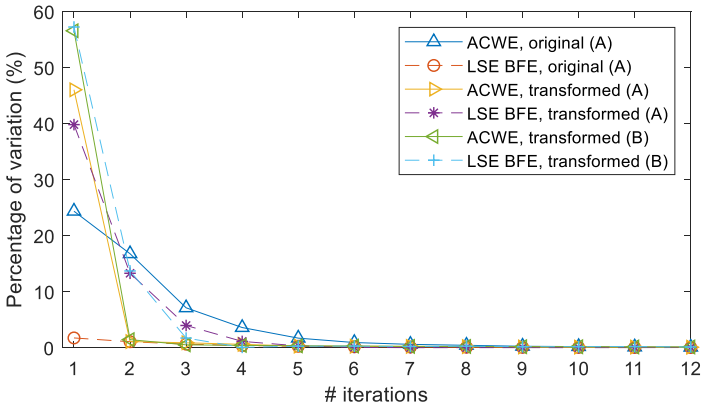

Fig. 11 – Percentage of pixel-wise variation of detected contours between i-th and (i-1)-th iterations of the ACWE and LSE BFE algorithms applied either to original images (lighting configuration A) or transformed images (lighting conditions A and B)

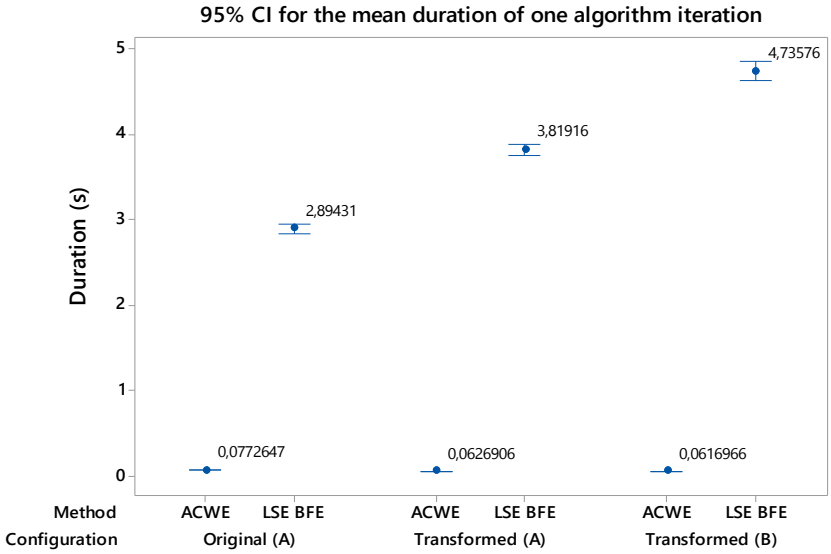

Fig. 12 – Duration of one iteration of the ACWE and LSE BFE algorithms applied either to original images (lighting configuration A) or transformed images (lighting conditions A and B)

6. CONCLUSIONS

In-situ sensing and monitoring methodologies represent key enabling technologies to make metal additive manufacturing processes able to meet stringent and challenging qualification requirements imposed by highly regulated industrial sectors. The layerwise production paradigm is well suited to in-situ monitoring as it offers the opportunity to gather a large amount of data while the part is being produced. This study was focused on the use of layerwise imaging combined with image segmentation algorithms to quickly detect major geometrical deviations during the process. This is particularly attracting from an industrial implementation viewpoint, as almost all industrial LPBF systems are equipped with cameras that capture images of the powder bed on a layer-by-layer basis. Although part dimensions and geometries measured in-situ are not representative of the final dimensions and geometry of the as-built part (because of shrinkage and thermal stress-induced distortions), if a major departure from the expected shape is observed in one layer, it represents an alarm that is worth signalling.

This study represents the first attempt to determine the accuracy and repeatability of in-situ measurements enabled by layerwise image processing and segmentation. To this aim, an experimental procedure that relies on the dimensional measurements of simple geometrical features was proposed. Two active contours segmentation methods were compared in the presence of several different lighting configurations, and the effects of the laser scan direction and image pre-processing operations were investigated as well.

The results showed that:

- For both the compared active contours methods, dark field illumination configurations produced the best segmentation and measurement performances, although a pre-processing operation based on the knowledge of the average pixel intensity of pre-scan images made both the methods more robust to illumination conditions;
- The segmentation results in the presence of most effective lighting configurations were robust to the laser scan direction;
- The ACWE and LSE BFE segmentation methods yielded statistically comparable measurement performances, although the ACWE is more computationally efficient and hence preferable from an in-situ implementation viewpoint. It is worth noting the ACWE computational efficiency does

not depend on lighting conditions and pre-processing operation, contrary to the LSE BFE approach;

- Under best lighting configurations, the pure error was an order of magnitude lower than the total variability: most of the variability depends then on the natural variability of the process, and not on the measuring instrument. Thus, the precision of the system in the identification of the dimension characteristics should be considered adequate to monitor the process;
- Under best lighting configurations, the total measurement variability was in the order of $80\ \mu m - 160\ \mu m$ for squared and circular shapes (about 1.6% – 3.2% of the nominal dimension), which is comparable to the shrinkage percentage of stainless steel parts, whereas the pure error was lower than $40\ \mu m$ (lower than about 0.8% of the nominal dimension);
- Worst results were achieved in the measurement of angles; in that case a higher pure error was observed. This issue requires additional investigations and an extension of the present study to more complex geometries;
- The measurements were affected by magnification and scale errors that produced different measurement biases along the X and Y axis: this is expected to be caused by a limited accuracy in the camera calibration procedure. This motivates the study of more effective calibration methods, possibly augmented by the results of the present performance characterization;
- The proposed image pre-processing operation allowed enhancing the measurement trueness in some cases with respect to the segmentation of original images, but it slightly inflated the pure error.

Future research will be aimed at extending these first achievements to more complex geometries and at investigating possible alternative sensing setups and image processing methodologies to further enhance the measurement performances. Moreover, grounding on the major findings of this study, an in-situ statistical monitoring approach for the detection of geometrical errors and layerwise defects can be developed. A future promising research direction consists of investigating image fusion methods to combine layerwise images acquired in the presence of different lighting configurations. A few seminal studies explored this possibility [7; 10; 25], but the characterization of resulting benefits in terms of measurement performance improvements still need to be quantified and analyzed. One additional research theme that deserves additional research

consists of combining image segmentation algorithms with surface topography reconstruction methods to improve the layerwise characterization.

ACKNOWLEDGEMENTS

This work was supported by European Union, Repubblica Italiana, Regione Lombardia and FESR for the project MADE4LO under the call "POR FESR 2014-2020 ASSE I - AZIONE I.1.B.1.3".

REFERENCES

[1] Gibson, I., Rosen, D. W., Stucker, B. (2010). Additive manufacturing technologies. New York: Springer.

[2] Horn, T. J., Harrysson, O. L. (2012). Overview of current additive manufacturing technologies and selected applications. Science progress, 95(3), pp. 255-282.

[3] Frazier, W. E. (2014). Metal additive manufacturing: A review. Journal of Materials Engineering and Performance, 23(6), pp. 1917-1928.

[4] Grasso M., Colosimo B.M., (2017), Process Defects and In-situ Monitoring Methods in Metal Powder Bed Fusion: a Review, Measurement Science and Technology, 28(4), 1-25

[5] Everton, S. K., Hirsch, M., Stravroulakis, P., Leach, R. K., & Clare, A. T. (2016). Review of in-situ process monitoring and in-situ metrology for metal additive manufacturing. Materials & Design, 95, 431-445.

[6] Mani, M., Lane, B., Donmez, A., Feng, S., Moylan, S., & Fesperman, R. (2015). Measurement Science Needs for Real-time Control of Additive Manufacturing Powder Bed Fusion Processes, NISTIR 8036, http://dx.doi.org/10.6028/NIST.IR.8036

[7] Abdelrahman, M., Reutzel, E. W., Nassar, A. R., & Starr, T. L. (2017). Flaw detection in powder bed fusion using optical imaging. Additive Manufacturing, 15, 1-11.

[8] Li, Z., Liu, X., Wen, S., He, P., Zhong, K., Wei, Q., … & Liu, S. (2018). In Situ 3D Monitoring of Geometric Signatures in the Powder-Bed-Fusion Additive Manufacturing Process via Vision Sensing Methods. Sensors, 18(4), 1180.

[9] Aminzadeh, M., & Kurfess, T. (2016). Vision-based inspection system for dimensional accuracy in powder-bed additive manufacturing. In ASME 2016 11th International Manufacturing Science and Engineering Conference (pp. V002T04A042-V002T04A042). American Society of Mechanical Engineers.

[10] Foster, B. K., Reutzel, E. W., Nassar, A. R., Hall, B. T., Brown, S. W., & Dickman, C. J. (2015) Optical, layerwise monitoring of powder bed fusion. In Solid Free. Fabr. Symp. Proc, 295-307.

[11] Kleszczynski, S., zur Jacobsmühlen, J., Sehrt, J. T., & Witt, G. (2012). Error detection in laser beam melting systems by high resolution imaging. In Proceedings of the Solid Freeform Fabrication Symposium.

[12] Zur Jacobsmühlen, J., Kleszczynski, S., Schneider, D., & Witt, G. (2013, May). High resolution imaging for inspection of laser beam melting systems. In 2013 IEEE International Instrumentation and Measurement Technology Conference (I2MTC) (pp. 707-712). IEEE.

[13] Zur Jacobsmühlen, J., Kleszczynski, S., Witt, G., & Merhof, D. (2015). Elevated Region Area Measurement for Quantitative Analysis Of Laser Beam Melting Process Stability. In Instrum. Meas. Technol. Conf. I2MTC (pp. 707-712).

[14] Caltanissetta, F., Grasso, M., Petrò S., Colosimo B.M. (2018) Layerwise Imaging for In-situ Monitoring of Geometrical Defects in Laser Powder Bed Fusion, EUSPEN's 18th International Conference & Exhibition, Venice, IT, June 2018

[15] Caltanissetta, F., Grasso, M., Petrò, S., Colosimo B.M. (2018), Layerwise Imaging for In-situ Metrology in Laser Powder Bed Fusion Process: A Preliminary Study, 2018 ASPE and EUSPEN Summer Topical Meeting, Advancing Precision in Additive Manufacturing, 22nd – 25th July 2018, Lawrence Berkeley National Laboratory Berkeley, California, USA

[16] Nixon, M. S., & Aguado, A. S. (2012). Feature extraction & image processing for computer vision. Academic Press.

[17] Blake, A., & Isard, M. (2012). Active contours: the application of techniques from graphics, vision, control theory and statistics to visual tracking of shapes in motion. Springer Science & Business Media.

[18] Baswaraj, D., Govardhan, A., & Premchand, P. (2012). Active contours and image segmentation: The current state of the art. Global Journal of Computer Science and Technology.

[19] Chan, T. F., & Vese, L. A. (2001). Active contours without edges. IEEE Transactions on image processing, 10(2), 266-277.

[20] Li, C., Huang, R., Ding, Z., Gatenby, J., Metaxas, D. N., & Gore, J. C. (2011). A level set method for image segmentation in the presence of intensity inhomogeneities with application to MRI. IEEE Transactions on Image Processing, 20(7), 2007.

[21] Land, W. S., Zhang, B., Ziegert, J., & Davies, A. (2015). In-situ metrology system for laser powder bed fusion additive process. Procedia Manufacturing, 1, 393-403.

[22] Zhang, B., Ziegert, J., Farahi, F., & Davies, A. (2016). In situ surface topography of laser powder bed fusion using fringe projection. Additive Manufacturing, 12, 100-107.

[23] Imani, F., Gaikwad, A., Montazeri, M. (2018a), Process Mapping and In-Process Monitoring of Porosity in Laser Powder Bed Fusion using Layerwise Optical Imaging, in press in the Journal of Manufacturing Science and Engineering, doi:10.1115/1.4040615

[24] Imani, F., Gaikwad, A., Montazeri, M., Yang, H., & Rao, P. (2018b). Layerwise in-process quality monitoring in laser powder bed fusion. ASME Paper No. MSEC, 6477.

[25] Gobert, C., Reutzel, E. W., Petrich, J., Nassar, A. R., & Phoha, S. (2018). Application of supervised machine learning for defect detection during metallic powder bed fusion additive manufacturing using high resolution imaging. Additive Manufacturing, 21, 517-528.

[26] Scime, L., & Beuth, J. (2018). Anomaly detection and classification in a laser powder bed additive manufacturing process using a trained computer vision algorithm. Additive Manufacturing, 19, 114-126.

[27] Aminzadeh, M. (2016). A machine vision system for in-situ quality inspection in metal powder-bed additive manufacturing(Doctoral dissertation, Georgia Institute of Technology).

[28] Sonka, M., Hlavac, V., & Boyle, R. (2014). Image processing, analysis, and machine vision. Cengage Learning.

[29] Kass, M., Witkin, A., & Terzopoulos, D. (1988). Snakes: Active contour models. International journal of computer vision, 1(4), 321-331.

[30] Unnikrishnan, R., Pantofaru, C., & Hebert, M. (2007). Toward objective evaluation of image segmentation algorithms. IEEE Transactions on Pattern Analysis & Machine Intelligence, (6), 929-944.

[31] Taha, A. A., & Hanbury, A. (2015). Metrics for evaluating 3D medical image segmentation: analysis, selection, and tool. BMC medical imaging, 15(1), 29.

[32] Zou, K. H., Warfield, S. K., Bharatha, A., Tempany, C. M., Kaus, M. R., Haker, S. J., ... & Kikinis, R. (2004). Statistical validation of image segmentation quality based on a spatial overlap index1: scientific reports. Academic radiology, 11(2), 178-189.

[33] Zitova, B., & Flusser, J. (2003). Image registration methods: a survey. Image and vision computing, 21(11), 977-1000.

[34] ISO 14405-1:2016, Geometrical product specifications (GPS) – Dimensional tolerancing, Part 1: Linear sizes, Second edition, 2016-08-15

[35] ISO 14405-3:2016, Geometrical product specifications (GPS) – Dimensional tolerancing, Part 3: Angular sizes, First edition, 2016-12-15

[36] Montgomery, D. C. (2017). Design and analysis of experiments. John wiley & sons.

[37] Mumford, D., & Shah, J. (1989). Optimal approximations by piecewise smooth functions and associated variational problems. Communications on pure and applied mathematics, 42(5), 577-685.

[38] Li, C., Xu, C., Gui, C., & Fox, M. D. (2010). Distance regularized level set evolution and its application to image segmentation. IEEE transactions on image processing, 19(12), 3243.

APPENDIX A

The underlying principle of active contour algorithms for image segmentation is based on the Mumford and Shah's minimization problem [19]. Let U_0 be the original grayscale image and let Ω be its domain, such that $U_0: \Omega \to \mathbb{R}$. The segmentation problem can be formulated in the following terms: find a decomposition of Ω into N sub-regions $\Omega_1, \Omega_2, \dots, \Omega_N$ such that an optimal piecewise smooth approximation U of U_0 varies

smoothly within each sub-region Ω_i and rapidly or discontinuously across the boundaries of Ω_i. Mumford and Shah [37] formalized this problem into the minimization of the following energy functional:

$$F^{MS}(U,C) = \int_{\Omega} (U_0 - U)^2 dxdy + \mu \int_{\Omega \backslash C} |\nabla U|^2 dxdy + \vartheta |C| \tag{A1}$$

where x and y are the coordinates of the pixels within the image, C is the contour of length $|C|$ corresponding to the desired segmentation defined as the union of the contours of all the sub-regions ($C = \bigcup_{i=1}^{N} C_i$), μ and ϑ and two weighting parameters and $\Omega \backslash C = \bigcup_{i=1}^{N} \Omega_i$.

The minimization of $F^{MS}(U,C)$ can be simplified by considering a piecewise constant approximation U such that $U_i = c_i$ for each $i = 1, \dots, N$, where c_i is a constant. Under this assumption, the Mumford-Shah minimization problem is called a "minimal partition problem" [19] and the energy functional becomes:

$$F^{MS}(U,C) = \sum_{i=1}^{N} \left(\int_{\Omega_i} (U_0 - c_i)^2 dxdy + \vartheta |C_i| \right) \tag{A2}$$

For a fixed contour C, the energy functional in (A2) is minimized by setting $c_i = mean(U_0)_{\Omega_i}$. The ACWE method proposed by Chan and Vese [19] simplifies the Mumford-Shah functional in the framework of the "minimal partition problem" as follows:

$$F^{MS}(c_1, c_2, C) = \int_{\Omega_1 = \omega} (U_0 - c_1)^2 dxdy + \int_{\Omega_2 = \Omega - \omega} (U_0 - c_2)^2 dxdy + \vartheta |C| + \mu A(C) \tag{A3}$$

where $A(C)$ is the area inside C and μ is the corresponding weighting term (i.e., a double penalization is envisaged, one on the area and one on the length of the identified contour). As a matter of fact, expression (A3) reduce the problem to a segmentation into only $N = 2$ sub-regions, where U_0 is approximated by a constant in each of them, with a penalization of the length of the contour. The traditional way to find the minimum of $F^{MS}(c_1, c_2, C)$ is based on the level set formulation, where the contour is defined as a level set

function: $C = \{(x, y)|\Phi(x, y) = 0\}$. Regarding the penalization of the contour length and area, Chan and Vese [19] proposed, as a default choice, setting $\mu = 0$, whereas the value of ϑ depends on the specific application.

The LSE BFE method proposed by Li *et al*. [20] is aimed at extending the region-based active contour methodologies to images characterized by pixel intensity inhomogeneity within the segmented areas. It combines the level set estimation with a bias field estimation. The underlying idea consists of replacing the energy functional proposed by Chan and Vese [19] with a local clustering criterion function for the intensities in a neighbourhood of each point. The local clustering criterion is integrated over the neighbourhood centre to define the new energy functional to be minimized, grounding on the level set formulation. This approach is based on the assumption that the observed image, U_0, can be modelled as follows:

$$U_0 = bJ + n \tag{A4}$$

where J is the true image, b is parameter that accounts of intensity inhomogeneity, labelled *bias field*, and n is an additive noise. The LSE BFE relies on the following assumptions: i) the bias field, b, is slowly varying, and hence it can be approximated by a constant in the neighbourhood of each point of the image domain; ii) the true image, J, approximately takes N distinct constant values $c_1, \dots, c_N$ in distinct regions $\Omega_1, \dots, \Omega_N$ that form the partition of the image; iii) the noise term is a zero-mean Gaussian noise with small variance.

Thus, differently from the ACWE method, the LSE BFE methodology attempts to estimate at the same time both the segmentation $\Omega \backslash \mathrm{C} = \cup_{i=1}^{N} \Omega_i$ corresponding to constants $c_1, \dots, c_N$ and the bias field, b.

In order to apply the local clustering criterion, the kernel trick is used. This leads to a modified formulation of the energy functional minimization problem where three coefficients must be selected: i) the contour length penalization coefficient, ϑ, ii) a regularization coefficient, μ, that replaces the penalization term $\mu A(C)$ in (A3) [38], and iii) the kernel width parameter. Li *et al*. [20] proposed the use of a truncated Gaussian kernel with width parameter σ and such that $\int K(\mathbf{x}) = 1$. This implies the selection of one further parameter, i.e., σ, with respect to the ACWE methodology.

APPENDIX B

The parameter μ was set to zero for both the methods: this is the default choice advocated by Chan and Vese [19], whereas Li *et al.* [20] demonstrated that the LSE BFE algorithm is not sensitive to the choice of that parameter. A sensitivity analysis for the choice of ϑ, i.e., the penalization coefficient applied to the contour length in the ACWE and LSE BFE algorithms, instead, was performed by referring to Build 1 data. For each illumination condition and for each segmentation method, the Dice's index was computed for $\vartheta \in [0.0001\ 100] \cdot 255^2$. The result was that the Dice's index was in most of the cases exactly constant within the entire interval, and only for few lighting conditions it exhibited a non statistically significant variation of the mean. This confirms previous findings in the literature that highlighted the robustness of the active contours methods here considered with respect to the choice of penalization coefficients [19 – 20]. In all the analysis presented in this study, the parameter ϑ was set to $0.001 \cdot 255^2$.

The choice of the kernel parameters in the LSE BFE formulation, instead, has a higher impact on the segmentation performances. According to Li *et al*. [20], a convolution kernel K was constructed as a $w \times w$ mask where w is the smallest odd number such that $w \geq 4\sigma + 1$, being K the Gaussian kernel of width σ. For each illumination condition and for each scan direction in Build 1, the Dice's index for the LSE BFE method applied either to the original or transformed images was computed for $\sigma \in [1\ 90]$. As an example, Fig. B1 shows the Dice's similarity index as a function of the kernel width, σ, for the LSE BFE algorithm applied to original images, just for specimens with scan direction equal to 0°. For sake of clarity, a subset of 10 illumination conditions was displayed in Fig. B1, as they are representative of dark field and bright field behaviours, respectively. For the first five dark field configurations, namely A, B, AL, AR and BL, quite high segmentation performances were achieved and they improved as σ increased, although above a given value of about $\sigma = 10$ no further improvement was achieved. For the five bright field configurations, namely D, DR, DL, AD and BCL, the segmentation goodness was lower and it exhibited a maximum at relatively low values of σ, i.e., $\sigma < 10$. This is in accordance with the findings of Li *et al*. [20], who pointed out that when less localized intensity inhomogeneities are present, larger values of σ should be preferred. Indeed, we observed that best segmentation quality was generally related to smoothest pixel intensity patterns within the foreground region, for which the σ selection procedure converged to higher values.

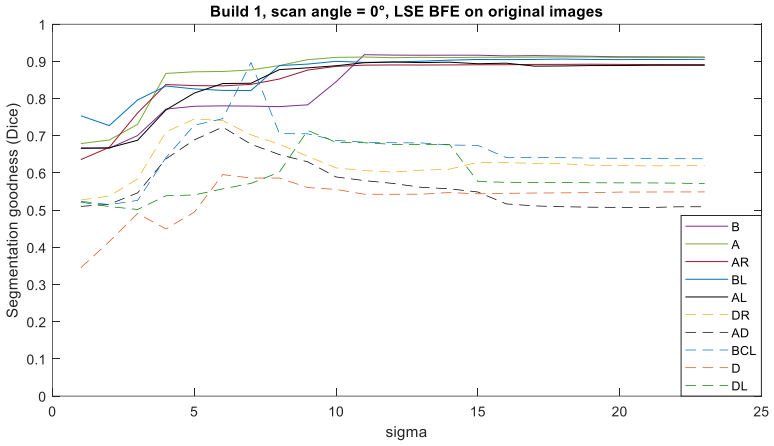

Fig. B1 – Example of average Dice's index values as a function of the kernel width parameter in the LSE BFE algorithm applied to original images in the presence of a subset of lighting conditions: dark field conditions are shown with continuous line, bright field conditions are shown with dashed line

Moreover, when the LSE BFE methodology was applied to transformed images, the selection of optimal kernel width values converged to significantly higher values than those obtained by applying the same method directly to the original images. Fig. B2 shows the 95% confidence intervals for the mean optimal σ in the two cases. This difference can be explained by the fact that the pre-processing operation (13) reduces the variation of pixel intensity within the foreground region and, as pointed out above, larger values of σ should be preferred in the presence of reduced localized intensity inhomogeneity.

In all the analysis presented in this study, the LSE BFE performances were always evaluated based on the corresponding optimal value of the σ parameter. No interaction effect was observed between σ and ϑ as far as the LSE BFE algorithm is concerned.

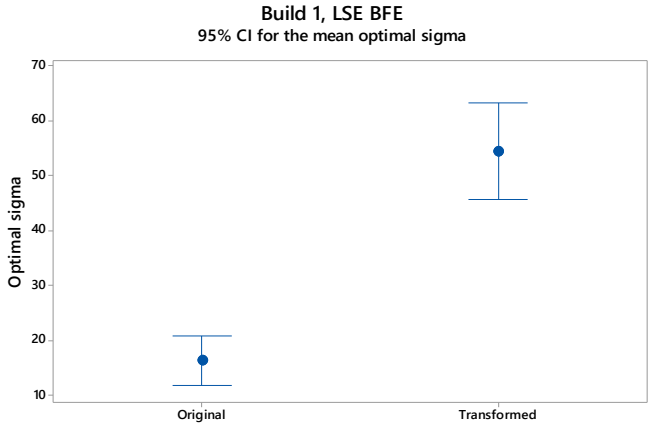

Fig. B2 – 95% confidence intervals for the mean kernel width parameter of the LSE BFE algorithm applied either to original or transformed images

APPENDIX C

Table C1 shows the p-values of the ANOVA tests used to investigate the existence of statistically significant effects of the scan direction on the Dice's index for different lighting conditions and for different segmentation algorithms.

Table C1 – p-values of ANOVA tests for the determination of statistical significance of the scan direction on the resulting Dice's index for different lighting conditions

Light conditions				p-values for "scan angle" factor			
				LSE BFE		ACWE	
	Vertical	Horizontal	ID	Original image	Transformed image	Original image	Transform. image
Dark field	None	Front	A	0,493	0,621	0,054	0,573
	None	Front	B	0,316	0,257	0,802	0,99
	Left	Front	AL	0,375	0,386	0,224	0,35
	Right	Front	AR	0,905	0,823	0,472	0,271
	Left	Front	BL	0,056	0,34	0,423	0,34
	Right	Front	BR	0,546	0,765	0,385	0,873
	Both	Front	BLR	0,369	0,792	0,493	0,732
Bright field	None	Back	C	0,311	0,404	0,162	0,206
	None	Back	D	0,443	0,241	0,749	0,599
	Left	Back	CL	0,183	0,322	0,341	0,331
	Right	Back	CR	0,859	0,991	0,993	0,99
	Left	Back	DL	0,44	0,28	0,492	0,485
	Right	Back	DR	0,054	0,866	0,42	0,432
	Both	Back	CLR	0,228	0,495	0,582	0,576
Other configurations	Left	Both	BCL	0,307	0,586	0,324	0,475
	Right	Both	BCR	0,577	0,848	0,564	0,849
	Both	Both	BCLR	0,479	0,507	0,257	0,652
	None	Both	AC	0,085	0,335	0,094	0,176
	None	Both	AD	**0,002**	**0,002**	**0,002**	**0,002**
	None	Both	BC	0,697	0,822	0,858	0,848
	None	Both	BD	**0**	**0,001**	**0**	**0**
	Left	None	L	0,677	0,522	0,374	0,562
	Right	None	R	0,042	0,655	0,296	0,875
	Both	None	LR	0,653	0,815	0,783	0,927